Retrieval of surface solar irradiance from satellite using machine learning: pitfalls and perspectives

Hadrien Verbois[1], Yves-Marie Saint-Drenan[1], Vadim Becquet[1], Benoit Gschwind[1], and Philippe Blanc[1]

[1]Mines Paris, Université PSL, Centre Observation Impacts Energie (O.I.E.), 06904 Sophia Antipolis, France

Correspondence: Hadrien Verbois (hadrien.verbois@minesparis.psl.eu)

Abstract. Knowledge of the solar surface irradiance (SSI) spatial and temporal characteristics is critical in many domains, the first of which is likely solar energy. While meteorological ground stations can provide accurate measurements of SSI locally, they are sparsely distributed worldwide. SSI estimations derived from satellite imagery are thus crucial to gain a finer understanding of the solar resource. To infer SSI from satellite images is, however, not straightforward and it has been the

5 focus of many researchers in the past thirty to forty years. For long, the emphasis has been on empirical models (simple parameterization linking the reflectance to the clear-sky index) and on physical models. Recently, new satellite SSI retrieval methods are emerging, which directly infer the SSI from the satellite images using machine learning. Although only a few such works have been published, their practical efficiency has already been questioned.

The objective of this paper is to better understand the potential and the pitfalls of this new coming family of methods. To

10 do so, simple multi-layer-perceptron (MLP) models are constructed with different training datasets of satellite-based radiance measurements from Meteosat Second Generation (MSG) with collocated SSI ground measurements from Meteo-France. The performance of the models is evaluated on a test dataset independent from the training set both in space and time.

We found that the data-driven model's performance is very dependent on the training set. On the one hand, even a simple MLP can significantly outperform a state-of-the-art physical retrieval method, provided the training set is sufficiently large and

15 similar enough to the test set. On the other hand, in certain configurations, the data-driven model can dramatically underperform even in stations located close to the training set.

1 Introduction

Spatial and temporal variabilities of solar surface irradiance (SSI) are of great interest across a range of fields, including climatology, solar energy, health, architecture, agriculture, and forestry. SSI estimations can be made using solar radiation

20 measurements from existing networks of meteorological ground stations. However, these are sparsely distributed worldwide. Imaging systems space-borne by meteorological geostationary satellites represent complementary upwelling radiance sources for SSI retrieval, as they enable better spatial and temporal coverage (Blanc et al., 2017; Müller and Pfeifroth, 2022; Tournadre, 2022). Since the eighties, multiple SSI retrieval approaches have been proposed using satellite images, from the earlier cloud index methods without explicit physical cloud models (Cano et al., 1986; Rigollier and Wald, 1998) to physics-based methods

25 with radiative transfer models (Xie et al., 2016; Qu et al., 2017). Statistical methods have also been developed to post-process

these retrieval models and correct their errors based on historical ground measurements (Polo et al., 2016, 2020; Huang et al., 2019). These correction algorithms, however, are mostly based on simple statistical methods and do not aim to replace the empirical and physical retrieval models upstream; in addition, most of the correction models proposed in the literature are local and therefore cannot generalize to locations they have not seen during training (Verbois et al., 2022).

30   In the past decade, Earth science has been revolutionized by the advent of machine and deep learning (Reichstein et al., 2019; Boukabara et al., 2019), with important developments in remote sensing (Ball et al., 2017), severe weather predictions (McGovern et al., 2017; Racah et al., 2017), and numerical weather modeling (Brenowitz and Bretherton, 2018; Rasp et al., 2018). In the field of SSI retrieval, new data-driven approaches are emerging based on automatic statistical learning, which attempt to infer a direct relationship between satellite images and SSI ground measurements. Papers presenting such retrieval

35   methods report promising performance (Jiang et al., 2019; Hao et al., 2019, 2020). However, a more thorough analysis is needed. In particular, the ability of machine learning-based models to generalize to new locations and specific meteorological and atmospheric events must be rigorously evaluated. Indeed, when Yang et al. (2022) evaluated the method proposed by Hao et al. (2019) outside the algorithm's training locations, they found that the method was performing significantly worse than expected.

40   In this work, we propose to further explore the potential of machine learning-based satellite-retrieval methods and to identify some of the main pitfalls that come with this type of approach. Our objective is not to propose a new retrieval method; we, therefore, implement a simple, purely machine-learning-based model. We, nonetheless, conduct a thorough and critical analysis of its performance and compare it with a state-of-the-art retrieval model, Heliosat 4 (Qu et al., 2017), operational as part of the Copernicus Atmosphere Monitoring Service (CAMS) radiation service.

45   The paper is organized as follows. In Section 2, we present the data used in this study. In Section 3, we describe our proposed machine-learning-based model. In Section 4, we set the stage for our analysis and present the experimental setups. The results are discussed in Section 5. Discussion and conclusion are given in Section 6.

2   Data

In this section, we briefly describe the data used in this study. Table 1 gives an overview.

Table 1. Overview of data used in this study.

Data	Time Sampling	Spatial resolution	Time extent	Spatial Extent	Source
SSI measurements	1 hour	Punctual	2010-2019	231 locations in France	Courtesy of Meteo-France
SSI measurements	1 minute	Punctual	2018-2019	Carpentras (FR)	BSRN Network
SSI estimations	1 hour	ca. 4x5 km	2018-2019	France	CAMS radiation services
CSI estimations	1 minute	ca. 4x5 km	2018-2019	France	CAMS radiation services
Climatic albedo	1 minute	ca. 4x5 km	2010-2019	France	CAMS radiation services
AOD measurements	1 minute	Punctual	2018-2019	Carpentras (FR)	Aeronet network

2.1 Satellite observation

We have been using readings of upwelling radiances L_λ from the multispectral optical imaging system aboard Meteosat second generation (MSG) meteorological geostationary satellite. MSG has 12 different channels, but we only use three of them here: two visible bands (centered on $0.6\ \mu m$ and $0.8\ \mu m$) and one infra-red band (centered on $10.8\ \mu m$). MSG channels have a temporal resolution of 15 minutes and a spatial resolution of 3 km at Nadir $(0,0)$[1], which above western Europe corresponds to pixels of ca. 4 by 5 km.

2.2 Ground measurements

2.2.1 Meteo-France stations

This study relies for training, validating, and testing on ground SSI measurements from 231 meteorological stations operated by Météo-France and spread over metropolitan France, as shown in Figure 2. The stations are equipped with Kipp&Zonen thermopile pyranometers[2] that measure 1-min Solar Surface Irradiance (SSI); here, however, we only have access to hourly averages. The data span a period of 9 years, between 2010 and 2019, but not all stations were operational during the whole period.

Strict quality checks (QC) are applied to the broadband data, as described extensively in (Verbois et al., 2023) and summarized in Appendix A. The idea is to select among all the ground measurement of SSI the ones that are the less questionable, both with commonly used automatic quality check procedures and expert visual-based scrupulous inspection, station per station, day per day.

The Météo-France station of Carpentras, included in the dataset described in Section 2.2.1, is also part of the BSRN (Ohmura et al., 1998) and Aeronet networks (Holben et al., 1998). As a BSRN station, it provides measurements of 1-min SSI. As an Aeronet station, it provides measurements of spectral aerosol optical depth (AOD). The AOD is only measured under clear-sky conditions; measurements are therefore not regular.

2.3 Copernicus Atmosphere Monitoring Services

The Copernicus Atmosphere Monitoring Service (CAMS) provides time series for various atmospheric and meteorological variables.

CAMS radiation service provides time series of global, direct, and diffuse ground irradiances. It relies on Heliosat 4, a state-of-the-art physical retrieval method (Qu et al., 2017) to infer ground irradiance from MSG satellites and CAMS atmospheric composition. CAMS estimations of SSI are used as a benchmark in this study. CAMS SSI natively comes with a resolution of 15 minutes, as it is derived from MSG. Here, however, we use hourly averages of SSI to match the resolution of the ground

---

[1]Except for the High-Resolution Visible (HRV) channel, which provides measurements with a resolution of 1 km, but on a reduced portion of the disk. This channel is not used in this study.

[2]The details of the instrument at each station can be found at: https://donneespubliques.meteofrance.fr/?fond=contenu&id$_{c}$ontenu $= 37$

data we use as a reference (Section 2.2.1).

CAMS also implements the McClear clear-sky model, which provides estimations of global, diffuse, and direct clear-sky irradiances. It is based on look-up tables from the radiative transfer model libRadtran and fed by partial aerosol optical depth, ozone and water vapor data from CAMS atmosphere services (Lefèvre et al., 2013; Gschwind et al., 2019). In this work, we use its global component, abbreviated CSI for clear-sky irradiance. As it will be used to detect clear-sky instants in Carpentras station, we use 1-minute values.

We also use the CSI hourly mean to compute clear sky index k_c from the SSI: $k_c = \frac{\text{SSI}}{\text{CSI}}$.

2.4 Ground albedo

The ground albedo is the fraction of the total irradiance reaching the surface of the earth that is reflected by the ground. In this work, we use the ground albedo to analyse the performance of the retrieval models. We rely on values derived from MODIS data sets (Blanc et al., 2014).

3 Machine learning based retrieval model

In this section, we present our proposed machine learning-based SSI satellite retrieval model – ML model in short. We describe the target and predictors in Section 3.1 and 3.2, respectively; the neural network architecture is detailed in Section 3.3. A code snippet showing the exact implementation of the network in TensorFlow is provided as supplementary material.

3.1 Target

The target of the model is the hourly Solar Surface Irradiance (SSI) and more precisely the global horizontal irradiance (GHI) component which is the downwelling shortwave surface flux. The ground truth, used for training the model and to evaluate its performance, is provided by the Météo-France measurement stations described in Section 2.2.1. To accelerate the training, the values are normalized by the corresponding average irradiance over the training period. The inverse transformation is applied to the network predictions before starting to analyze its performance.

3.2 Predictors

The choice of predictors is critical in statistical learning. Because we use a simple fully connected network (Section 3.3), we want to keep the dimensions of the predictor set relatively low, while giving as much context as possible to the algorithm. We are also restricted by the fact that ML model must be fully online and can therefore only utilize past and present data. To estimate the SSI in each location (with latitude x and latitude y) at a given time t, predictors from 4 sources are used.

The main inputs to ML model come from satellite measurements. We use the upwelling radiances $L_{0.6\mu m}$, $L_{0.8\mu m}$, and $L_{10.8\mu m}$, described in Section 2.1. To give the model as much spatial and temporal context as possible, 9 neighboring pixels

and 13 preceding 15-min time steps are used as input. This corresponds to a zone of 12 by 15 km and a period of 3 hours. In summary, for a point with latitude and longitude (x, y) at time t_0, such as the closest satellite pixel has coordinates (i_0, j_0), the following predictors are taken from MSG data:

$$L_\lambda(i, j, t) \text{ for } i, j \in [i_0 - 1, i_0 + 1] \times [j_0 - 1, j_0 + 1]$$

$$t \in [t_0 - 12dt, t_0], \text{ where } dt = 15 \ min$$

$$\lambda \in \{0.6 \ \mu m, 0.8 \ \mu m, 10.8 \ \mu m\}$$

The solar azimuth angle ψ_s and the solar elevation γ_s , computed using the sg2 python library (Blanc and Wald, 2012), are also provided as predictors. They define the topocentric angular position of the Sun. The day of the year and the hour of the day are given as predictors too. Finally, the latitude and longitude, as well as the corresponding altitude are used as predictors.

In total, the model has 358 predictors, summarized in Table 2. Each predictor is normalized and centered. These 358 predictors are concatenated in a single 1D vector which is used as input to the neural network.

Table 2. Predictors used to estimate SSI at given time and place.

Name	Dimension	Source
Satellite $L_{0.6 \ \mu m}$	$3 \times 3 \times 13 = 117$	MSG
Satellite $L_{0.8 \ \mu m}$	$3 \times 3 \times 13 = 117$	MSG
Satellite $L_{10.8 \ \mu m}$	$3 \times 3 \times 13 = 117$	MSG
Solar position: elevation and azimuth angles	2	sg2 (Blanc and Wald, 2012)
Hour of the day and day of the year	2	Calendar
Location and altitude	3	BSRN

3.3 The machine learning model: a fully connected network

As discussed in introduction, the aim of this work is not to propose a new optimized retrieval model, but to investigate the advantage and drawbacks of purely ML-based models. We therefore implement a *classic* algorithm: a fully connected neural network (FCN), or Multiple Layer Perceptron (MLP). This model has been around for many years and has proven very powerful in many fields and industries. It is not, however, the state-of-the-art in machine learning: *deep* architectures optimized for e.g. images or time-series have since been developed and outperform FCN for complex spatio-temporal problems. As we will see in this paper, a simple FCN is nonetheless sufficient to at least partially solve the satellite retrieval challenge.

Our FCN has the following configuration:

- one hidden layer of 64 neurons, for a total of 23,041 parameters.

- The hidden layer uses a relu activation function, the last neuron uses a linear activation function.

- The weights are initialized randomly using a normal distribution.

– The loss function is the mean square error (mse).

The same configuration, but with two and three hidden layers was also tested. As they had similar (validation) performance, we preferred the simpler configuration.

The network is trained using the RMSprop algorithm with learning rate=0.001, rho=0.9, momentum=0.0, and epsilon=1e-07 (Griffin et al., 2003). Regularization is implemented through an early stopping procedure, which stop training if the validation

135   error does not decrease for more than 20 epochs.

Because the last layer uses a linear activation function, there is no guarantee that the predicted value is positive. To ensure we do not get any negative SSI estimation, any negative prediction is set to 0.

The random initialization of the network weights slightly impacts the network performance. The impact on the model

140   performance is, however, limited, as discussed in Appendix B. In this study, each model was trained 20 times, with different (randomly assigned) initial weights, and present the results for the worse performing model (in terms of test mse) in the rest of the manuscript. Choosing the best performing one – or any of the 20 runs – would lead to very similar results and the same conclusions.

4   Experiments setup

145   In this section, we describe the setup of the experiments conducted in this study. In Section 4.1, we introduce the metrics used to assess the performances of the SSI estimations; in Section 4.2, we discuss the splitting of the data into training and test sets; finally, in Section 4.3, we describe the clear-sky detection method used in the result Section 5.2.

4.1   Performance metrics

The SSI estimations produced by the ML model, $\hat{x}_{ML}$, as well as the SSI estimation from CAMS, $\hat{x}_{CAMS}$, are compared with

150   the ground measurements x of SSI from Météo-France stations. Both datasets have a resolution of 1-hour.

Three different error metrics are used, namely, the root mean square error RMSE, the mean bias error MBE and the standard deviation of the error SDE:

$$\text{RMSE} = \sqrt{\frac{1}{n}\sum\nolimits_{k=1}^{n}(\hat{x}_k - x_k)^2} \tag{1}$$

$$\text{MBE} = \frac{1}{n}\sum\nolimits_{k=1}^{n}(\hat{x}_k - x_k) \tag{2}$$

155   $$\text{SDE} = \sqrt{\frac{1}{n}\sum\nolimits_{k=1}^{n}(\hat{x}_k - x_k - \text{MBE})^2} \tag{3}$$

where n is the number of points and $\hat{x}_k \in \{\hat{x}_k^{ML}, \hat{x}_k^{CAMS}\}$. MBE measures the accuracy – or bias – of the estimations, SDE their precision, and RMSE is a combination of both. The three metrics are related as follows: $\text{RMSE}^2 = \text{MBE}^2 + \text{SDE}^2$

The correlation between $\hat{x}$ and x is also a popular metric. To compare estimations to measurements, and quantify the performance of a model, we use Pearson correlation coefficient $\rho_{pearson}$. Because it measures linear correlation, the Pearson

correlation is, however, not appropriate to unveil non-linear relationships between two time-series. To quantify the strength and direction of association between two time-series, we thus prefer Spearman's Rank-Order Correlation, $\rho_{spearman}$ (Spearman, 1987).

To compare the performance of ML model and CAMS, we sometimes use the RMSE skill score, taking CAMS as a reference:

$$\text{Skill} = 1 - \frac{\text{RMSE}_{ML}}{\text{RMSE}_{CAMS}} \tag{4}$$

It corresponds to opposite of the relative difference between RMSE_{ML} and RMSE_{CAMS}. A positive Skill means that $\text{RMSE}_{ML} < \text{RMSE}_{CAMS}$ i.e., that the ML model outperforms CAMS in terms of RMSE.

4.2 Training, validation, and test set

Splitting the data into a test and training set is a crucial step in machine learning studies. Machine learning models, such as neural networks, can achieve exceptional performance on data that is similar to the data used for their training. However, their performance may deteriorate drastically when they operate outside their training space (Hastie et al., 2009). The model's ability to generalize to new, unseen data is a crucial metric of its performance. The definition of what constitutes data outside the training space depends on the specific problem at hand, as it varies based on how the model will be used in practice. The training and test set must therefore be selected carefully to ensure the model's suitability for deployment in practical applications.

In this study, we evaluate a satellite retrieval model, which is meant to provide accurate SSI estimations in any location – at least within a certain region – and at any (future) time. We must thus ensure that ML model generalizes in time and space. To that end, we use different locations for training and testing and reserve the period 2018-07-01 to 2019-06-30 for testing while only data from 2010-01-01 to 2018-06-30 is used for training. The setup, adapted from Verbois et al. (2022), is illustrated in Figure 1.

How we assign measurement stations to one set or the other is also important and will test the ability of the model to generalize in space differently. In this study, we test three training setups, with different objectives in mind:

- Training setup 1, described in Section 4.2.1, allows us to evaluate the ability of the model to generalize in space when training and test stations are geographically intertwined.

- Training setup 2, described in Section 4.2.2, allows us to understand the sensitivity of the model performance to the density of training stations, when they are still intertwined with the test stations.

- Training setup 3, described in Section 4.2.3, enforces a geographical separation between training and test stations and thus allows us to test the ability of the model to generalize to locations geographically outside its training space.

For each training setup, a validation set is needed for early stopping (Section 3.3). In all three setups, $max(10, 0.2 \times$ (number of training stations)) stations are randomly chosen in the training set to constitute the validation set.
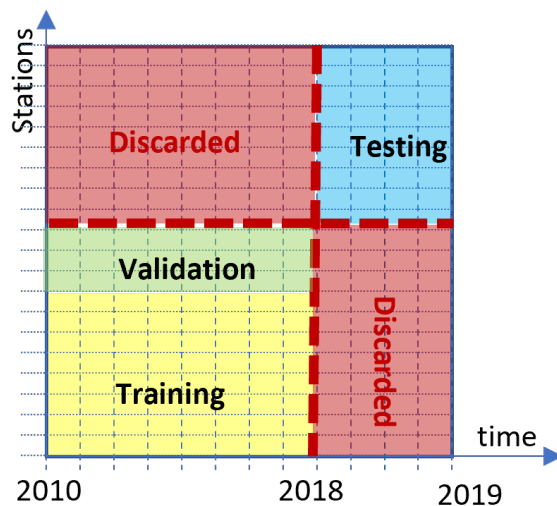
Figure 1. Training, validation and test sets, after Verbois et al. (2023).
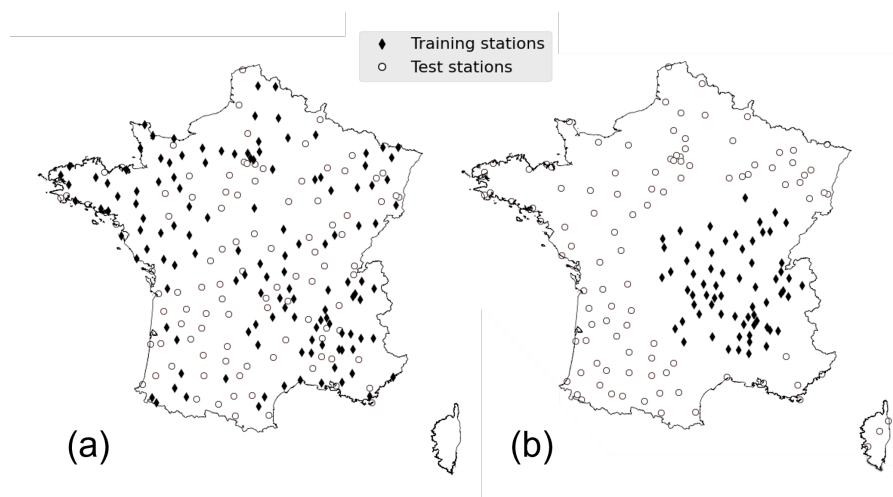
Figure 2. Distribution of train and test stations for training setups 1 and 2 (a) and training setup 3 (b).

4.2.1 Training setup 1

In the first setup, 100 test stations are chosen randomly from those passing QC for more than 30% of the hours over the test period (2018-07-01 to 2019-06-30). Note that, since night-time is flagged as failing QC, 30% is a high requirement. All the remaining stations that pass QC for more than 30% of the hours over the training period (2010-01-01 to 2018-06-30) are used as training stations – there are 129 of them. Three tricks are applied:

 – The 100 test stations are chosen as a priority among the stations that do not pass QC for the training period. That is to maximize the number of stations used.

 – The Carpentras station is manually added to the test set; that is because it is part of the Aeronet and BSRN networks (see Section 2.2) and can thus be used for a more thorough analysis of the models' performance.

 – The three meteorological stations located in Corsica, an island 160 km from the shores of Metropolitan France are not considered in this use case.

The resulting training and test stations are shown in Figure 2.a.

4.2.2   Training setup 2

The second setup is very similar to setup 1. The same 100 stations make up the test set, but only N stations are picked for training. N varies from 20 to 100. There are $\binom{129}{N}$ ways to choose N training stations among 129 candidates, and the performance of the model is likely impacted by this choice, especially with low N. However, training with every possible combination is not computationally tractable[3]; instead, we randomly pick 20 combinations for each N.

4.2.3   Training setup 3

In the third setup, we enforce geographical separation between the training and test set. All the stations within a circle of center 46°N, 4°E and of radius 215 km passing QC for more than 30% of the hours over the training period (2010-01-01 to 2018-06-30) are taken as training stations, and all stations outside of a circle of center 46° N, 4° E and radius 255 km passing QC for more than 30% of the hours over the test period (2018-07-01 to 2019-06-30) are used as test stations. This separation is somewhat arbitrary, the objective is to keep enough stations in the training set while concentrating them in a region as small as possible. This results in 66 training stations and 105 test stations, as illustrated in Figure 2.b.

4.3   Clear sky detection

In Section 5.2, we focus our analysis on days with a majority of clear-sky instants. It is difficult to accurately detect clear-sky instants with mean hourly SSI; we, therefore, restrict the analysis to the station of Carpentras, for which we have minute data (Section 2.2). We first detect clear-sky minutes with a 1-minute resolution, using the Reno and Hansen algorithm (with a window length of 10 minutes) (Reno and Hansen, 2016) implemented in the pvlib python library (F. Holmgren et al., 2018). We then select days for which 75% of the daytime is detected as clear sky.

---

[3] $max\left(\binom{129}{N}\right) \approx 4.8 \times 10^{37}$ $(N = 65)$

5 Results

This results section is divided into three parts. In Section 5.1, we analyze the general performance of ML model with training setup 1, for the whole test period. In Section 5.2, we still work with training setup 1, but focus on the specific case of clear-sky days for the station of Carpentras. Finally, in Section 5.3, we discuss the impact of the number and location of training stations on the performance of ML model (training setups 2 and 3).

5.1 Model performance with a dense training set

In this section, we analyze the performance of ML model with training setup 1, i.e. using the maximum number of randomly chosen training stations (129). Although training and test stations are different, they are largely interlaced (Figure 2.a).

5.1.1 Overall performances

We first evaluate ML model and CAMS performance metrics for all 100 test stations and the whole test period. The overall metrics are shown in Table 3. ML model has a significantly lower RMSE and SDE than CAMS – 19% and 18% respectively. The correlation between ML model and the ground measurements is higher than that between CAMS and the ground measurements. In terms of bias, on the other hand, the difference between the two retrieval models is negligible: both MBE are relatively low.

Table 3. Overall test metrics for CAMS and ML Model with training setup 1 (computed over 391481 samples).

	ML model (training setup 1)	CAMS
RMSE (Wm^{-2})	52.92	64.99
MBE (Wm^{-2})	52.28	64.02
SDE (Wm^{-2})	-8.21	-11.22
$\rho_{pearson}$	0.977	0.966

To better understand the characteristics of ML model and CAM estimations, we look at the joint distribution between estimations and ground measurements, shown in Figures 3.a and 3.b. As suggested by ML model lower SDE, the joint distribution of this model is more tightly wrapped around the axis x=y than that of CAMS. In addition, the joint distribution does not show any artifact or un-physical features – as is sometimes the case for e.g. overly smooth estimations or forecasts (Verbois et al., 2020).

The distribution of SSI – estimated or measured – is highly dominated by the diurnal and annual pattern of the Sun. To focus on the ability of the retrieval models to resolve clouds, we compare the clear-sky indices from the estimations and from the ground measurements in Figure 3.c (ML model) and Figure 3.d (CAMS) by analyzing their joint distribution. Overall, ML model estimations of the clear-sky index are more likely to be close to the ground measurements. In addition, by design, CAMS estimations of the clear-sky index never take a value outside the interval $[0.1, 1]$, whereas ML model better matches the

distribution of the ground measurements, with the clear-sky index values ranging from 0 to 1.8. Admittedly, ML model tends to produce too many estimations with high the clear-sky index. Furthermore, CAMS seems to handle situations for which the clear-sky is close to one better than ML model; this point will be further discussed in Section 5.2.
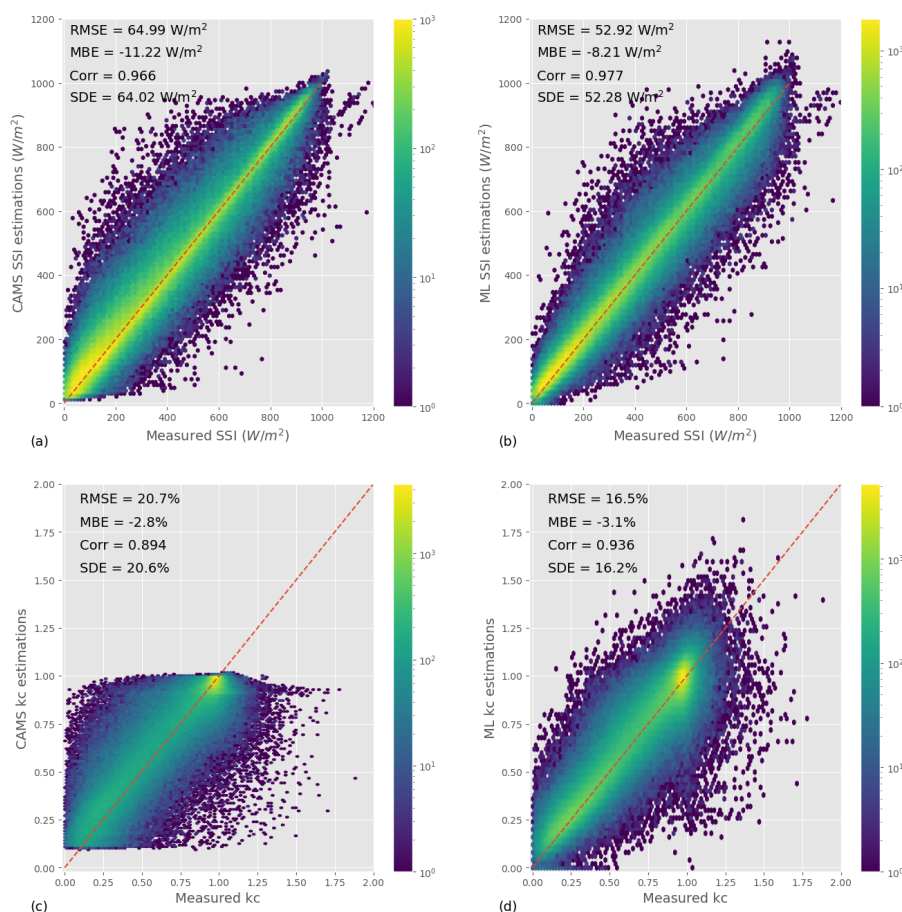
Figure 3. Joint distributions of satellite-derived estimations and ground measurements, for ML model (a and c) and for CAMS (b and d).

5.1.2 Station-wise performances

Beyond the overall performance, a retrieval model needs to be consistent. We, therefore, analyze ML model and CAMS performances for each test station independently. Figure 4 compares the RMSE, SDE, and MBE of the two models for each station: one point in the graph corresponds to one station and the green band identifies stations for which ML model is better than CAMS. We see that in terms of RMSE, ML model outperforms CAMS for all but 4 stations. Furthermore, the difference between the two models for these 4 stations is small. In terms of SDE, ML model does even better, as it outperforms CAMS in 98% of the test stations. In terms of bias, interestingly, ML model has a higher MBE than CAMS for 58% of the stations, even

255 though its overall MBE was lower than that of CAMS. In addition, although CAMS and ML model have a low MBE overall, it reaches 50 Wm^{-2} in some locations, which is not negligible.
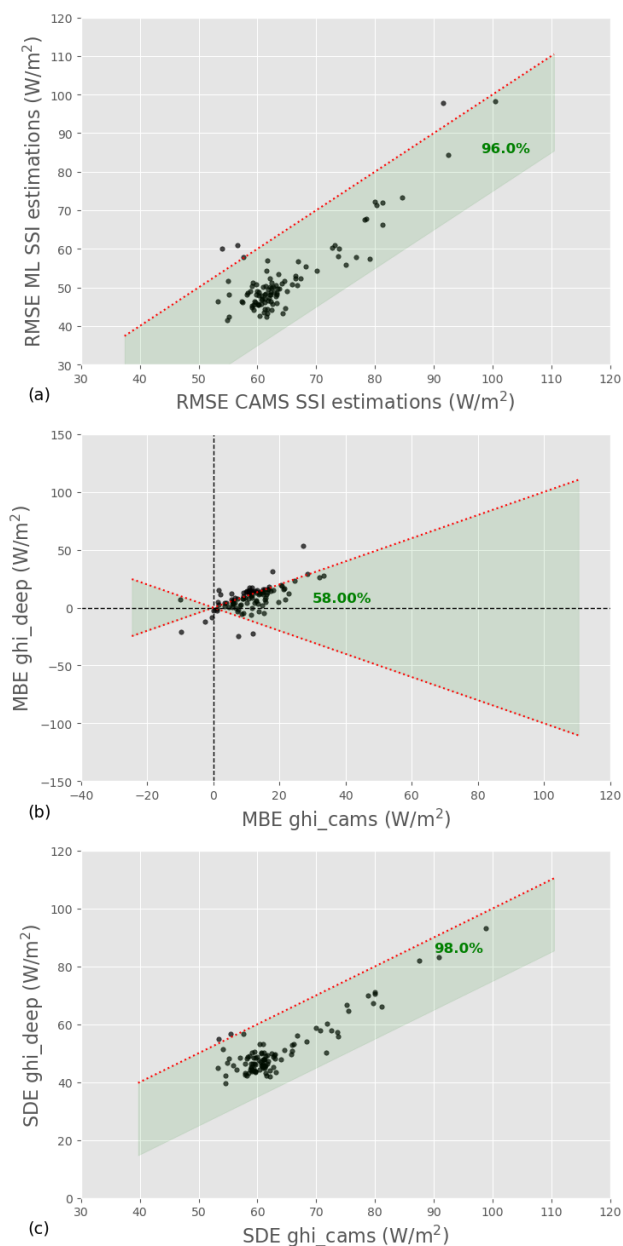
Figure 4. Comparison of RMSE (a), MBE (b) and SDE (b) of ML model and CAMS for each station. The green band indicates for which stations ML model outperforms CAMS; the corresponding percentage is indicated in bold green.

5.1.3 Performance analysis with respect to different conditions

To complete our analysis of the two models' overall performances, we look at the metrics' dependence on the sky conditions. We use the clear-sky index as a proxy: low clear-sky index corresponds to overcast skies, high clear-sky index to clear skies, and intermediate clear-sky index to partly cloudy skies. This is certainly an oversimplification, and a more sophisticated analysis would be required for an accurate classification of the sky conditions; having access to the hourly average of SSI, however, the value of clear-sky index is a good first approximation. The station-wise RMSE, SDE, and MBE of ML model and CAMS are broken down per class of clear-sky index in Figure 4; boxplots are used to represent the metric's spread across stations (each boxplot is built with 100 points: one for each test station). We showed in Section 5.1.1 that ML model has a lower RMSE and SDE than CAMS; we see here that it is mostly for low clear-sky indices that ML model outperforms CAMS. For clear-sky indices larger than 0.9, both retrieval models have similar RMSE, and CAMS even has a slightly lower SDE in that clear-sky index interval. In terms of bias, although both models have similar MBE overall (Table 3), their dependence on k_c is different. CAMS overestimates the SSI for low clear-sky indices and underestimated it at high clear-sky indices; ML model, on the contrary, systematically overestimates the SSI, but to a lesser extent.

5.2 Specific case of clear-sky days

The previous section should have convinced us that with training setup 1, ML model significantly and systematically outperforms CAMS in mainland France and under all-sky conditions. Figure 3 and Figure 5, however, suggest that things may be different under clear-sky conditions. Furthermore, SSI retrieval from satellite observations notably involves specific considerations when there are no clouds: aerosol concentrations and ground albedo, for example, have a stronger impact on empirical and physical estimations in cloudless skies (Scheck et al., 2016).

In this section, we focus on the performance of the two retrieval models under clear sky conditions. To clearly identify such conditions, we need 1-minute irradiance data (Section 4.3); we thus focus on the Carpentras station (Section 2.2). Note that the ML model is the same as the one discussed in Section 5.1; only the analysis is restricted to one location.

5.2.1 Clear sky performances

The performance metrics of ML model and CAMS for all skies and clear sky days are shown in Table 5.2.1. As expected, ML model has a lower RMSE and SDE than CAM for all skies; it even has a slightly lower MBE. For clear sky days, both models have a significantly lower RMSE and SDE. But, on the contrary to the general case, CAMS significantly outperforms ML model in all metrics, with RMSE, SDE and MBE 27%, 26%, and 57% lower, respectively.

Several factors could explain the deficiency of ML model under clear skies. In cloudless conditions, the albedo of the ground plays a more important role than under cloudy skies; since ML model has no information about this quantity, it could be one source of uncertainty. Aerosols and in particular aerosols optical depth (AOD) are also important under clear skies; CAMS, through the clear sky model McClear, accounts for AOD in its estimations, but ML model has no direct access to this information.
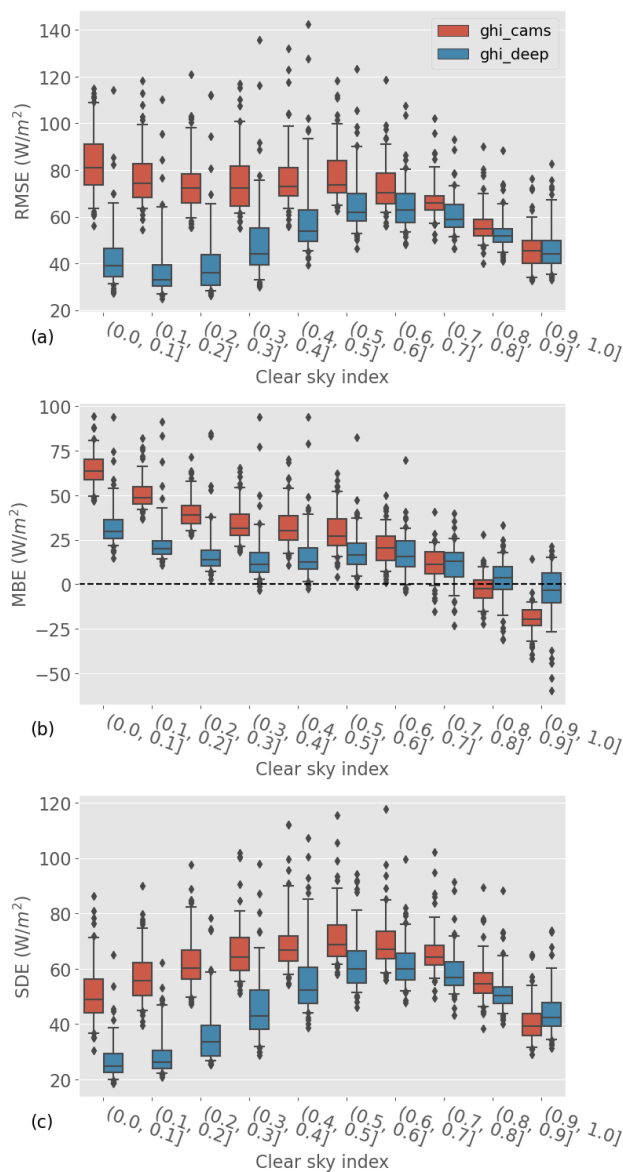
Figure 5. Distribution of station RMSE (a), MBE (b) and SDE (b) of ML model and CAMS as a function of the clear-sky index k_c. Each boxplot is built with 100 points: one for each test station.

5.2.2 Impact of aerosols

290   Albedo variations are most often more significant in space, while AOD varies in both space and time. Because we perform the clear-sky specific analysis in a single location, it is difficult to investigate the impact of albedo on the clear-sky performance. We therefore focus in this section on the impact of aerosol on CAMS and ML model clear sky estimations.

Table 4. Performance of ML model and cams for Carpentras stations under all skies (4012 samples) and under clear skies only (938 samples).

		ML model (training setup 1)	CAMS
All skies	RMSE (Wm^{-2})	42.31	55.09
	MBE (Wm^{-2})	-3.31	7.40
	SDE (Wm^{-2})	42.18	54.59
	$\rho_{pearson}$	0.987	0.978
Clear sky days	RMSE (Wm^{-2})	21.82	15.95
	MBE (Wm^{-2})	-4.92	-2.07
	SDE (Wm^{-2})	21.27	15.81
	$\rho_{pearson}$	0.996	0.999

Figure 6.a shows the AOD at 500 nm measured at the Carpentras station for two consecutive clear-sky days. We chose these dates as illustration, because a significant drop in AOD can be observed from one day to the next. The corresponding measurements of hourly SSI are shown by black crosses in Figure 6.b. Even though both days have a clear sky profile, the SSI values are significantly higher for the second day, particularly in the middle of the day. CAMS estimations of SSI for that day, shown on the same figure in red, match the observations very well: the model rightfully integrates the effect of aerosols. ML model, in blue in the figure, correctly estimates two clear sky days, but the values of SSI for the two days are nearly identical: as suspected, ML model is not able to account for the effect of aerosol as well as CAMS.

To further investigate the role of information about AOD at 500 nm in ML model under-performing for clear-sky days, Figure 7 shows the distribution of the error of each retrieval model as a function of AOD 500; the corresponding Spearman correlation is also displayed. Although there is no obvious pattern, the error of ML model appears to have a relationship with AOD 500, as confirmed by the relatively high Spearman correlation. CAMS error, on the other hand, is weakly correlated with AOD 500. Even though correlation is not causation, this result further supports the hypothesis that not accounting for AOD 500 in ML model causes some of the estimations error under clear sky.

5.3 Sensitivity to the training set

To this point, we have analyzed the performance ML model with training setup 1, i.e. when the neural network is trained with 129 stations, interlaced with the test stations (Figure 2.a). Such a density of measurement stations is rare, and many of the regions covered by MSG – and thus by CAMS – are not as well equipped. In this section, we therefore evaluate the impact of the size and location of the training set on the performance of ML model. We first reduce the number of training stations while keeping the random split (training setup 2 - Section 4.2.2) and then enforce geographical separation between training and test stations (training setup 3 - Section 4.2.3). In this section, we focus on RMSE for conciseness.
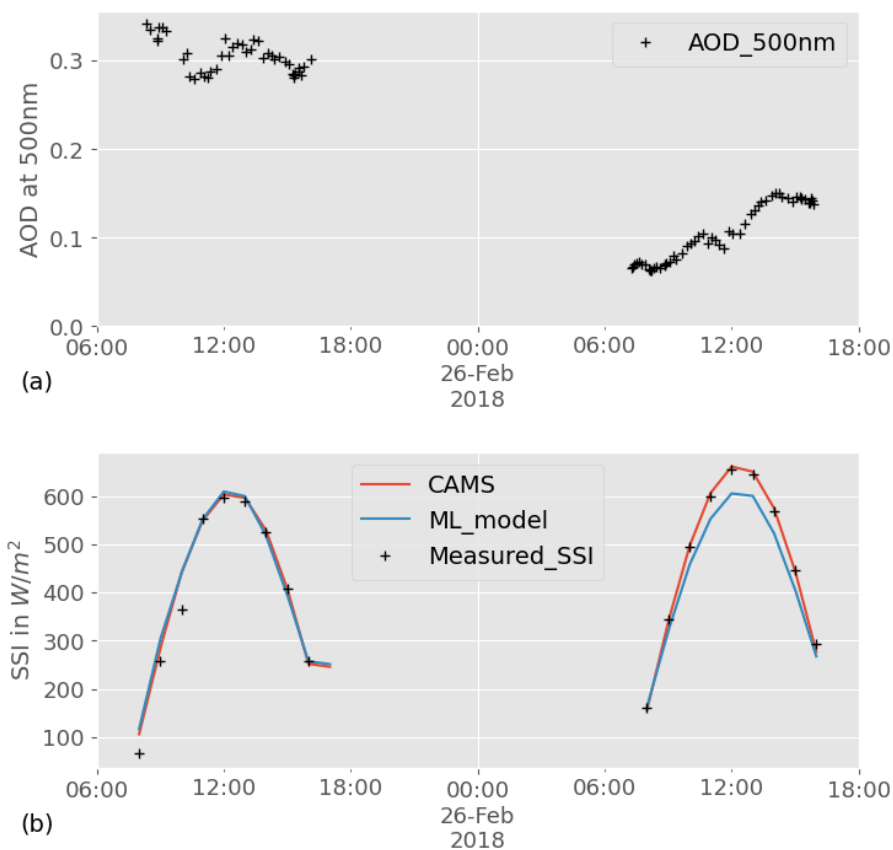
Figure 6. Example of two consecutive clear-sky days (with aerosols) Carpentras.

5.3.1 Impact of the number of training stations

ML model is trained here with training setup 2 (Section 4.2.2). Figure 8 shows the RMSE of ML model for the 100 test stations
315 as a function of the number of training stations N. As discussed in Section 4.2.2, we repeat the experiment 20 times for each
choice of N, with different randomly chosen training stations at each iteration. For $N = 129$, as there are only 129 candidates,
the 20 iterations are done with the same training stations. The variations of the RMSE for $N = 129$ are thus only caused by the
variations in the random initialization of the weights between runs, discussed in Appendix B.

For $N \geq 40$, the RMSE of ML model remains significantly lower than that of CAMS, even though it increases a bit on
320 average for $N \leq 100$. For $N = 20$, however, ML model performances deteriorate markedly: the RMSE of the best-performing
run is higher than for $N \geq 40$, and the RMSE of the worse-performing run largely exceeds that of CAMS. We also notice that
the RMSE variations between runs is more important for $N = 20$; this suggest that the issue is not as much the size of the
training set, but the location of the training stations.
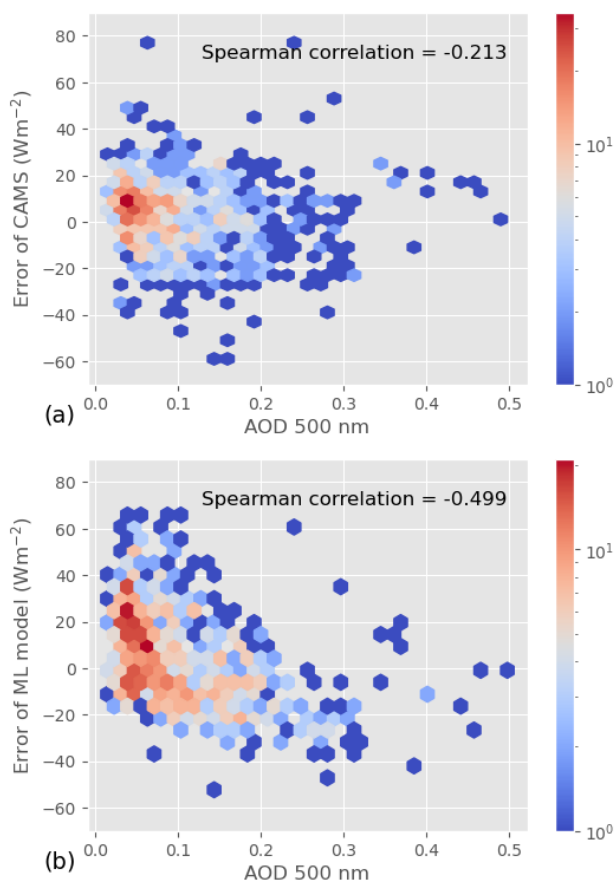
Figure 7. Joint distribution of AOD and estimation error for CAMS (a) and ML model (b). Spearman's Rank-Order Correlation between AOD and error is also given.

5.3.2 Impact of the location of the training stations

325 To further investigate the impact of the relative location of the training and test stations on ML model performances, we enforce a geographical separation between them (training setup 3 - Section 4.2.3)[4]. Table 5 shows the overall metrics for ML model and CAMS. The performance of the latter is similar to the one described in Section 5.1, even though we use different test stations. Contrastingly, the RMSE and SDE of ML model are much higher with this training setup than they were with training setup 1 or 2 (with N≥40). Whereas ML model was outperforming CAMS with training setup 1, the average performances of the two 330 retrieval models are almost equivalent here.

As in Section 5.1.3, it is interesting to analyse the performances per station. Figure 9 compares the RMSE of ML model and CAMS for each station. We see that while the two retrieval models have similar RMSE on average, the distributions of

---

[4]It should be noted that the test stations are not the same as in training setup 1 and 2; the values of RMSE, MBE, SDE or $\rho_{pearson}$ should thus not be compared with previous sections.
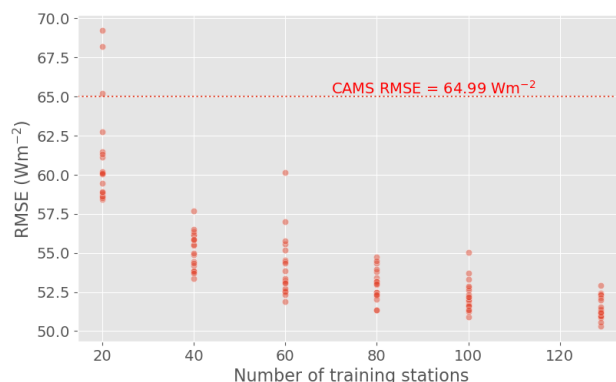
Figure 8. Test RMSE as a function of the number N of stations used for the training with 20 random picks of N among 129 (training setup 2).

Table 5. Overall test metrics for CAMS and ML Model with training setup 3 (computed over 411733 samples).

	ML model (training setup 3)	CAMS
RMSE (W.m^{-2})	61.04	63.49
MBE (W.m^{-2})	-6.69	10.25
SDE (W.m^{-2})	60.68	62.66
$\rho_{pearson}$	0.969	0.967

the station-wise RMSE are very different. ML model RMSE is slightly lower for 82 of the 105 test stations, while CAMS performs somewhat better for 18 other stations. For 3 to 5 locations, however, ML model RMSE is dramatically higher than that of CAMS: in the worst case, RMSE$_{\text{ML model}}$ is more than two times higher than RMSE$_{CAMS}$.

5.3.3 Impact of Albedo

We have shown that, with geographical separation between training and testing sets (training setup 3), ML model performs reasonably well on average but is susceptible to providing highly inaccurate estimations in some locations. To try and understand what causes highly inaccurate estimations, the geographical distribution of test RMSE skill is represented in Figure 10. Interestingly, the distance to the training set does not have a clear impact on the performance of ML model. Rather, most of the stations for which ML model is largely outperformed by CAMS (i.e. with high negative skill scores) are located on the Mediterranean or Atlantic coasts. Ocean and continental tiles have different albedos, which significantly impacts the radiance observed by the satellite (Blanc et al., 2014). Physical and empirical retrieval models account for that difference, but ML model does not have direct access to that information; this could explain its poor performance in seaside stations.

To test that hypothesis, Figure 11.b shows the RMSE skill score of each test station as a function of its mean albedo. We observe that while a negative skill score does not necessarily imply a low albedo, a low albedo (lower than 0.1) systematically
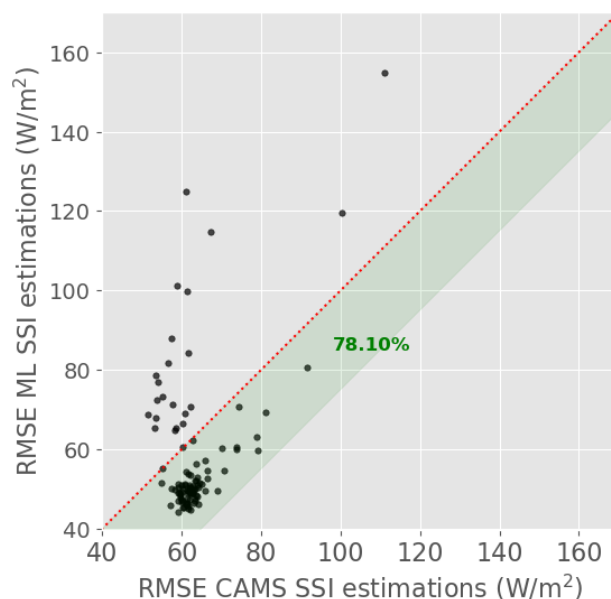
Figure 9. Comparison of RMSE of ML model (training setup 3) and CAMS for each station. The green band indicates for which stations ML model outperforms CAMS; the percentage of such station is indicated in bold green.

comes with a negative skill score. The existence of a positive relationship between albedo and RMSE skill score is further supported by a statistically significant Spearman correlation coefficient of 0.348 between the two values. Figure 11.a shows the same plot but for training setup 1. We see that in this case, low albedo does not come with negative RMSE skill score. This absence of relationship – or at least its lower strength compared to training setup 3 – is confirmed by a statistically non-significant ($p = 0.07$) Spearman correlation coefficient of 0.184 between the RMSE skill score and the albedo.

To understand the difference of behavior between the two training setups, it is useful to look at the distribution of the albedo for training stations in either case; the mean albedo of training stations are hence shown on the y=0 axis in Figure 11. In training setup 1, several training stations have a mean albedo between 0.025 and 0.1, while in training setup 3, all training stations' albedo are greater than 0.1. This suggests that the RMSE skill score is not directly influenced by the test station albedo, but rather by the distance between test stations albedo and training stations albedo. In other words, ML model is not able to generalize to stations with an albedo it hasn't seen during training.

6 Discussions and Conclusions

6.1 With a dense training set, great potential with some reserves

Machine learning for satellite retrieval has great potential. Provided we have the right data, performance improvement over traditional approaches can be important. We indeed showed that, when trained with a network of measurements stations spread
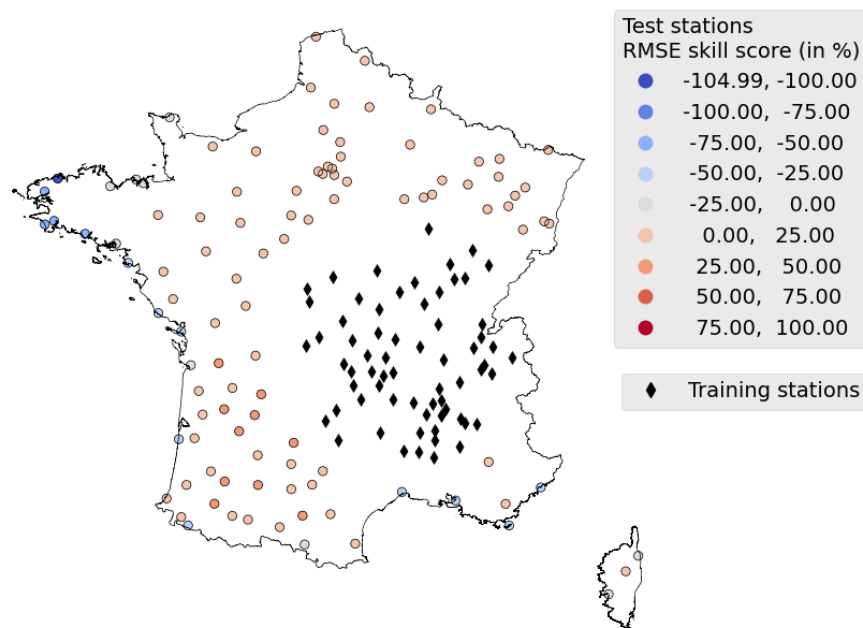
Figure 10. Geographical distribution of the RMSE skill score of ML model in training setup 3. Positive values show the stations where ML model outperforms CAMS.

evenly across France, a simple neural network has significantly lower error metrics and better overall representativity than CAMS, a state-of-the-art physical retrieval model. Because we ensured that we tested the ability of the model to extrapolate in space and time, that means that such a model could be used operationally and, on average, provide better estimations than CAMS.

We found, however, that the neural network is not able to fully account for the role of Aerosols in clear-sky estimations, whereas CAMS underlying model – as well as other empirical or physical models – can. This lack of representativity of physical phenomena slightly impacts the performance but, more critically, it undermines the confidence in the model.

6.2 Strong dependence on training set

Our results show that the model's performance is very dependent on the training set. First, we found that even a simple network – with only one hidden layer – requires a relatively large number of training stations to outperform CAMS. In many regions, good quality ground-measurements are likely too scarce for this model to be useful.

We further demonstrated that, rather than the number of training stations, their location relative to the test sites is crucial. Our analysis showed that, in certain configurations, the neural network can underperform even in stations located close to the training set. We know that neural networks often have difficulty making predictions out of the training domain; the challenge here is that determining which location is out of the training domain is not straightforward. Whether two locations are similar
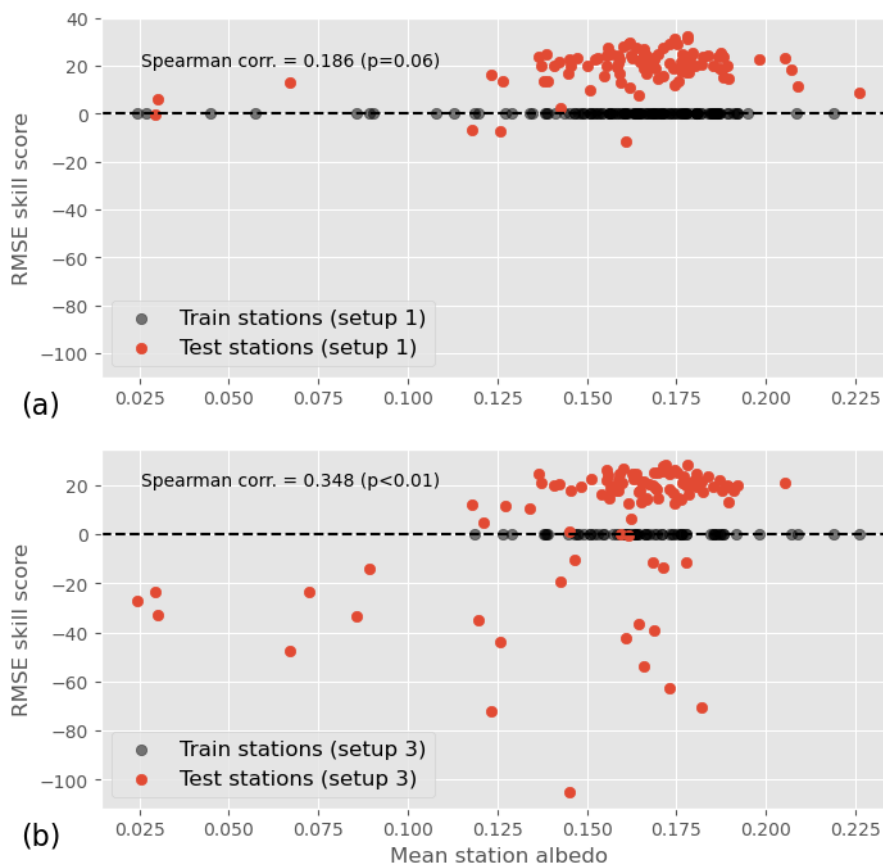
Figure 11. RMSE skill score as a function of station mean albedo for training setup 1 (a) and training setup 3 (b). The distribution of the training stations' albedo is also shown on the y=0 axis.

in the eye of the network does not depend directly on the geographical distance between these locations. Our analysis suggests that its albedo may play a role in the ability of the neural network to generalize to a location, but it is likely not the only cause.

6.3 Perspectives

380 Third-generation geostationary satellites are already operational above the Untied State (GOES-R) and Japan (Himawari-8), while Meteosat Thid-Generation will soon cover Europe and Africa. These new meteorological satellites have better temporal, spatial and spectral resolutions than their second-generation counterparts. They thus produce a significantly larger amount of data. To treat these data operationally and fully benefit the additional information, deep learning certainly has a critical role to play.

385   However, the solar research community needs to address the limitations of purely statistical models, as revealed in this paper. We believe that the answer resides at least partly in hybrid models, mixing physical modelling and statistical learning.

Variations of hybrid models include the use of machine learning models trained on datasets derived from physical simulations. These models can serve as proxies for parts of existing physical models and can be further fine-tuned on real datasets via transfer learning. This approach balances the incorporation of underlying physical principles with considerations of real-world complexities and uncertainties. Another approach is to design machine learning models with physical constraints incorporated as regularization, such as conservation laws and material properties. This can ensure that the model stays within the realm of physical possibility while also incorporating data-driven components. A third option could be the direct incorporation of physical equations into the loss function of the machine learning model. This approach optimizes the model's predictions to be both data-driven and physically consistent. During the training process, the model is guided by both observed data and underlying physical laws.

A better understanding of the generalization capabilities of the models is also critical. We saw in this paper that the albedo may play a role, but more research is needed to understand to what extent and in which conditions we can expect the model to generalize well. Data segmentations algorithms could be useful to optimize the construction of training datasets, and to identify locations where the retrieval model may not be trusted.

Data availability. The following data sources are accessible online for free:

- CAMS estimates of solar surface irradiances and clear sky irradiances can be downloaded from the soda website: https://www.soda-pro.com/help/cams-services/cams-radiation-service/download-europe-volume or with the following pvlib function: https://pvlib-python.readthedocs.io/en/stable/reference/generated/pvlib.iotools.get_cams.html

- MSG data is available on the Eumetsat website: https://www.eumetsat.int/access-our-data

- Ground irradiance data for Carpentras station can be downloaded from the BSRN website: https://bsrn.awi.de

Meteo-France data was generously provided by Meteo-France for research purpose. More information can be found on the Meteo-France public data website: https://donneespubliques.meteofrance.fr

Appendix A: Quality check

The quality check procedure applied to Meteo-France ground measurements is described in detail in Verbois et al. (2023). In summary, it consists of the following checks:

1. Each value is tested for *extremely rare limits* (ERL) as recommended by Long and Dutton (2010):

$$-2 < GHI < 1.2 I_{sc} cos^{1.2}(\theta_z) + 50 \text{Wm}^{-2}$$

   where I_{sc} is the solar constant adjusted for Earth-Sun distance, and θ_z the solar zenith angle.

2. A digital model of the horizon (Blanc et al., 2011) is used to exclude every instant for which the sun is under the horizon.

3. A visual check on the spatial coherence of k_c is performed.

   4. A visual check for shadow is performed in the solar azimuth - solar elevation plan.

415   Out of the original 286 stations available, 46 are fully exculded by QC.

Appendix B: Performance variations due to random initialization

Figure B1 shows the RMSE, MBE and SDE of 20 models ran with exactly the same setup - described in Section 3.3, but different randomly chosen weight initialization. SDE and RMSE vary between 50-52 Wm^{-2}, and 50-53 Wm^{-2} respectively; This is relatively small compared to CAMS, that has a RMSE of 64.9 Wm^{-2} and an SDE of 64 Wm^{-2}. The MBE, on the other

420   hand, varies between 0 and 9 Wm^{-2}. That is more important compared to CASM MBE (ca 12 Wm^{-2}), but still relatively mall compared to the average SSI in France.
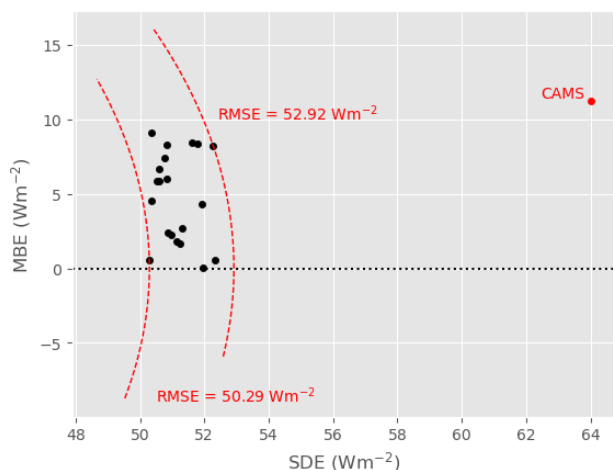
Figure B1. Target diagram showing the RMSE, MBE and SDE of 20 models ran with exactly the same setup, but different weight initialization.

Author contributions. Conceptualization and Methodology were done by HV, YMSD and PB. Data curation was done by YMSD and BG. Software was done by HV and BG. Formal analysis and visualisation were done by HV and VB. Original draft preparation was done by HV. Review & editing was done by YMSD, VB, BG and PB.

425   *Competing interests.* The authors declare that they have no conflict of interest.

Acknowledgements. The work of Hadrien Verbois, Yves-Marie Saint-Drenan, Vadim Becquet, and Philippe Blanc was supported by the SciDoSol chair.

References

Ball, J. E., Anderson, D. T., and Chan, C. S.: Comprehensive survey of deep learning in remote sensing: theories, tools, and challenges for
430   the community, Journal of Applied Remote Sensing, 11, 1, https://doi.org/10.1117/1.jrs.11.042609, 2017.

Blanc, P. and Wald, L.: The SG2 algorithm for a fast and accurate computation of the position of the Sun for multi-decadal time period, Solar
Energy, 86, 3072–3083, https://doi.org/10.1016/j.solener.2012.07.018, 2012.

Blanc, P., Gschwind, B., Lefèvre, M., and Wald, L.: The HelioClim project: Surface solar irradiance data for climate applications, Remote
Sensing, 3, 343–361, https://doi.org/10.3390/rs3020343, 2011.

435   Blanc, P., Gschwind, B., Lefevre, M., and Wald, L.: Twelve monthly maps of ground Albedo parameters derived from MODIS data sets,
International Geoscience and Remote Sensing Symposium (IGARSS), pp. 3270–3272, https://doi.org/10.1109/IGARSS.2014.6947177,
2014.

Blanc, P., Remund, J., and Vallance, L.: Short-term solar power forecasting based on satellite images, Elsevier Ltd,
https://doi.org/10.1016/B978-0-08-100504-0.00006-8, 2017.

440   Boukabara, S.-A., Krasnopolsky, V., Stewart, J. Q., Maddy, E. S., Shahroudi, N., and Hoffman, R. N.: Leveraging Modern Artificial Intel-
ligence for Remote Sensing and NWP: Benefits and Challenges, Bulletin of the American Meteorological Society, 100, ES473–ES491,
https://doi.org/10.1175/BAMS-D-18-0324.1, 2019.

Brenowitz, N. D. and Bretherton, C. S.: Prognostic Validation of a Neural Network Unified Physics Parameterization, Geophysical Research
Letters, 45, 6289–6298, https://doi.org/10.1029/2018GL078510, 2018.

445   Cano, D., Monget, J., Albuisson, M., Guillard, H., Regas, N., and Wald, L.: A method for the determination of the global solar radiation from
meteorological satellite data, Solar Energy, 37, 31–39, https://doi.org/10.1016/0038-092X(86)90104-0, 1986.

F. Holmgren, W., W. Hansen, C., and A. Mikofski, M.: pvlib python: a python package for modeling solar energy systems, Journal of Open
Source Software, 3, 884, https://doi.org/10.21105/joss.00884, 2018.

Griffin, M. K., Burke, H.-h. K., Mandl, D., and Miller, J.: Cloud cover detection algorithm for EO-1 Hyperion imagery, in: In-
450   ternational Geoscience and Remote Sensing Symposium (IGARSS), edited by Shen, S. S. and Lewis, P. E., vol. 1, p. 483,
https://doi.org/10.1117/12.487297, 2003.

Gschwind, B., Wald, L., Blanc, P., Lefèvre, M., Schroedter-Homscheidt, M., and Arola, A.: Improving the McClear model estimat-
ing the downwelling solar radiation at ground level in cloud-free conditions - McClear-v3, Meteorologische Zeitschrift, 28, 147–163,
https://doi.org/10.1127/metz/2019/0946, 2019.

455   Hao, D., Asrar, G. R., Zeng, Y., Zhu, Q., Wen, J., Xiao, Q., and Chen, M.: Estimating hourly land surface downward
shortwave and photosynthetically active radiation from DSCOVR/EPIC observations, Remote Sensing of Environment, 232,
https://doi.org/10.1016/j.rse.2019.111320, 2019.

Hao, D., Asrar, G. R., Zeng, Y., Zhu, Q., Wen, J., Xiao, Q., and Chen, M.: DSCOVR/EPIC-derived global hourly and daily down-
ward shortwave and photosynthetically active radiation data at $0.1° \times 0.1°$ resolution, Earth System Science Data, 12, 2209–2221,
460   https://doi.org/10.5194/essd-12-2209-2020, 2020.

Hastie, T., Tibshirani, R., and Friedman, J.: The Elements of Statistical LearningData Mining, Inference, and Prediction, Second Edition,
Springer Series in Statistics, Springer New York, New York, NY, https://doi.org/10.1007/978-0-387-84858-7, 2009.

Holben, B. N., Eck, T. F., Slutsker, I., Tanré, D., Buis, J. P., Setzer, A., Vermote, E., Reagan, J. A., Kaufman, Y. J., Nakajima, T., Lavenu, F., Jankowiak, I., and Smirnov, A.: AERONET - A federated instrument network and data archive for aerosol characterization, Remote

465   Sensing of Environment, 66, 1–16, https://doi.org/10.1016/S0034-4257(98)00031-5, 1998.

Huang, G., Li, Z., Li, X., Liang, S., Yang, K., Wang, D., and Zhang, Y.: Estimating surface solar irradiance from satellites: Past, present, and future perspectives, Remote Sensing of Environment, 233, 111 371, https://doi.org/10.1016/j.rse.2019.111371, 2019.

Jiang, H., Lu, N., Qin, J., Tang, W., and Yao, L.: A deep learning algorithm to estimate hourly global solar radiation from geostationary satellite data, Renewable and Sustainable Energy Reviews, 114, 109 327, https://doi.org/10.1016/j.rser.2019.109327, 2019.

470   Lefèvre, M., Oumbe, A., Blanc, P., Espinar, B., Gschwind, B., Qu, Z., Wald, L., Schroedter-Homscheidt, M., Hoyer-Klick, C., Arola, A., Benedetti, A., Kaiser, J. W., and Morcrette, J. J.: McClear: A new model estimating downwelling solar radiation at ground level in clear-sky conditions, Atmospheric Measurement Techniques, 6, 2403–2418, https://doi.org/10.5194/amt-6-2403-2013, 2013.

Long, C. N. and Dutton, E. G.: BSRN Global Network recommended QC tests, V2.x, 2010.

McGovern, A., Elmore, K. L., Gagne, D. J., Haupt, S. E., Karstens, C. D., Lagerquist, R., Smith, T., and Williams, J. K.: Using artificial

475   intelligence to improve real-time decision-making for high-impact weather, Bulletin of the American Meteorological Society, 98, 2073–2090, https://doi.org/10.1175/BAMS-D-16-0123.1, 2017.

Müller, R. and Pfeifroth, U.: Remote sensing of solar surface radiation-a reflection of concepts, applications and input data based on experience with the effective cloud albedo, Atmospheric Measurement Techniques, 15, 1537–1561, https://doi.org/10.5194/amt-15-1537-2022, 2022.

480   Ohmura, A., Dutton, E. G., Forgan, B., Frohlich, C., Gilgen, H., Hegner, H., Heimo, A., Konig-Langlo, G., Mcarthur, B., Miiller, G., Philipona, R., Pinker, R., Whitlock, ', C. H., Dehne, K., and Wild, M.: Tech. rep., 1998.

Polo, J., Wilbert, S., Ruiz-Arias, J. A., Meyer, R., Gueymard, C., Súri, M., Martín, L., Mieslinger, T., Blanc, P., Grant, I., Boland, J., Ineichen, P., Remund, J., Escobar, R., Troccoli, A., Sengupta, M., Nielsen, K. P., Renne, D., Geuder, N., and Cebecauer, T.: Preliminary survey on site-adaptation techniques for satellite-derived and reanalysis solar radiation datasets, Solar Energy, 132, 25–37,

485   https://doi.org/10.1016/j.solener.2016.03.001, 2016.

Polo, J., Fernández-Peruchena, C., Salamalikis, V., Mazorra-Aguiar, L., Turpin, M., Martín-Pomares, L., Kazantzidis, A., Blanc, P., and Remund, J.: Benchmarking on improvement and site-adaptation techniques for modeled solar radiation datasets, Solar Energy, 201, 469–479, https://doi.org/10.1016/j.solener.2020.03.040, 2020.

Qu, Z., Oumbe, A., Blanc, P., Espinar, B., Gesell, G., Gschwind, B., Klüser, L., Lefèvre, M., Saboret, L., Schroedter-Homscheidt, M., and

490   Wald, L.: Fast radiative transfer parameterisation for assessing the surface solar irradiance: The Heliosat-4 method, Meteorologische Zeitschrift, 26, 33–57, https://doi.org/10.1127/metz/2016/0781, 2017.

Racah, E., Beckham, C., Maharaj, T., Kahou, S. E., Prabhat, and Pal, C.: ExtremeWeather: A large-scale climate dataset for semi-supervised detection, localization, and understanding of extreme weather events, Advances in Neural Information Processing Systems, 2017-Decem, 3403–3414, 2017.

495   Rasp, S., Pritchard, M. S., and Gentine, P.: Deep learning to represent subgrid processes in climate models, 115, 1–6, https://doi.org/10.1073/pnas.1810286115, 2018.

Reichstein, M., Camps-Valls, G., Stevens, B., Jung, M., Denzler, J., Carvalhais, N., and Prabhat: Deep learning and process understanding for data-driven Earth system science, Nature, 566, 195–204, https://doi.org/10.1038/s41586-019-0912-1, 2019.

Reno, M. J. and Hansen, C. W.: Identification of periods of clear sky irradiance in time series of GHI measurements, Renewable Energy, 90,

500   520–531, https://doi.org/10.1016/j.renene.2015.12.031, 2016.

Rigollier, C. and Wald, L.: Towards operational mapping of solar radiation from Meteosat images, Proceedings of the EARSeL Symposium 1998 "operational remote sensing for sustainable development", pp. 385–391, 1998.

Scheck, L., Frèrebeau, P., Buras-Schnell, R., and Mayer, B.: A fast radiative transfer method for the simulation of visible satellite imagery, Journal of Quantitative Spectroscopy and Radiative Transfer, 175, 54–67, https://doi.org/10.1016/j.jqsrt.2016.02.008, 2016.

505 Spearman, C.: The Proof and Measurement of Association between Two Things, The American Journal of Psychology, 100, 441, https://doi.org/10.2307/1422689, 1987.

Tournadre, B.: Heliosat-V : une méthode polyvalente d'estimation du rayonnement solaire par satellite, Tech. rep., https://pastel.archives-ouvertes.fr/tel-03227271, 2022.

Verbois, H., Blanc, P., Huva, R., Saint-Drenan, Y.-M. Y. M., Rusydi, A., and Thiery, A.: Beyond quadratic error: Case-study of a multiple
510 criteria approach to the performance assessment of numerical forecasts of solar irradiance in the tropics, Renewable and Sustainable Energy Reviews, 117, 109 471, https://doi.org/10.1016/j.rser.2019.109471, 2020.

Verbois, H., Saint-Drenan, Y. M., Thiery, A., and Blanc, P.: Statistical learning for NWP post-processing: A benchmark for solar irradiance forecasting, Solar Energy, 238, 132–149, https://doi.org/10.1016/j.solener.2022.03.017, 2022.

Verbois, H., Saint-Drenan, Y.-M. M., Quentin, L., Yann, M., Marie, C., Laurent, D., and Blanc, P.: Improvement of satellite-derived surface
515 solar irradiance estimations using spatio-temporal extrapolation with statistical learning, Under Review, 2023.

Xie, Y., Sengupta, M., and Dudhia, J.: A Fast All-sky Radiation Model for Solar applications (FARMS): Algorithm and performance evaluation, Solar Energy, 135, 435–445, https://doi.org/10.1016/j.solener.2016.06.003, 2016.

Yang, X., Bright, J. M., Gueymard, C. A., Acord, B., and Wang, P.: Worldwide validation of an Earth Polychromatic Imaging Camera (EPIC) derived radiation product and comparison with recent reanalyses, Solar Energy, 243, 421–430,
520 https://doi.org/10.1016/j.solener.2022.08.013, 2022.